Progress In Electromagnetics Research, PIER 63, 171–191, 2006

SIMULATIONS OF THE LEFT-HANDED MEDIUM USING DISCONTINUOUS GALERKIN METHOD BASED ON THE HYBRID DOMAINS

Y. Shi and C.-H. Liang

School of Electronic Engineering
Xidian University
Xi'an, Shaanxi 710071, P. R. China

Abstract—The increasing interest in electromagnetic effects in the Left-Handed medium (LHM) requires the formulae capable of the full analysis of wave propagation in such materials. First, we develop a novel technique for discretization of the Lorentz medium model. In order to overcome the instability inherent in the standard perfectly matched layer (PML) absorbing boundary condition (ABC), we derive the modified PML ABC which can be extended to truncate the boundary of LHM. Then a convergent high-order accurate scheme based on triangle domains, discontinuous Galerkin method (DGM), is extended to the new DGM based on hybrid domains, triangle domains and quadrilateral domains. Finally, we adopt the new DGM and modified PML formulations to analysis the electromagnetic phenomena in the LHM. The simulation results show accuracy and stability of the proposed scheme.

1. INTRODUCTION

It has been demonstrated recently that a substance studied theoretically by Veselago [1], in which the dielectric constant ε and magnetic permeability μ are both negative, can be attained artificially in a metamaterial represented by a periodic medium of metallic wires [2] and split-ring resonators (SRR's) [3] that is characterized by an effective permittivity ε_{eff} and permeability μ_{eff} that can both have negative values in a certain frequency range. Remarkably, simultaneously negative material parameters lead to opposite directions of the Poynting vector and phase velocity vector of plane waves propagating in the material, which shows the existence of backward waves in double-negative (DNG) media. Three vectors $\vec{E}$, $\vec{H}$

and $\vec{k}$ form the left-handed triplets in DNG media, so such materials have been termed left-handed media (LHM).

Up to now, both theoretical and experimental efforts [4–7] have focused on the study of the dispersion relations of permittivity and permeability. A periodic array of the thin wire medium is represented by the frequency-dependent dielectric function

$$\varepsilon_{eff}(\omega) = 1 - \frac{\omega_p^2}{\omega^2} \tag{1}$$

in which ω_p is the plasma frequency, which depends on the geometrical parameters of the wires in a manner that allows scaling down ω_p to microwave frequencies. On the other hand, an array of split ring resonators exhibits behavior that can be described by an effective frequency-dependent permeability in the form

$$\mu_{eff}(\omega) = 1 - \frac{F\omega^2}{\omega^2 - \omega_0^2 + i\omega\Gamma} \tag{2}$$

The finite-difference time-domain (FDTD) method is used to numerically simulate the LHM by most of researchers because of its simple scheme. Ziolkowski et al. [8] has adopted the FDTD method to directly solve Maxwell's equations in order to study unusual EM phenomena in the LHM. Davi et al. [9] has extended Ziolkowski's approach to simulate three-dimensional wave propagation problems in the LHM. However, numerous examples have indicated that a sampling density of at least 10–20 cells per minimum wavelength is necessary to ensure that the FDTD method produces acceptable results even for a small problem. For a large-scale problem, the time window of interest is usually longer. Since the dispersion error is linear proportional to the length of time integration, in order to maintain an acceptable accuracy, the sampling rate must be increased accordingly. In addition, simulations of properties and applications of the LHM require the proper absorbing boundary condition (ABC) capable of being extended to truncate the boundary of LHM. Among them, the perfectly matched layer (PML) introduced by Berenger [10] has been the most popular ABC. However, standard versions of PML [10, 11] are inherently unstable when it is extended to truncate the boundary of LHM without any modification.

In order to efficiently solve time-domain electromagnetic problems, many researchers have proposed various techniques to improve the FDTD method. Recently, the discontinuous Galerkin methods (DGM) have attracted much attention of researchers. Being higher order versions of traditional finite volume method [12], the DGM were

developed initially in 1970's for the study of neutron transport equations [13], and have now been applied to the area of computational fluid dynamics and the solution of Maxwell's equations [14–17]. Discontinuous Galerkin methods can obtain better accuracy and less phase error in solving wave propagations due to the adoption of high order polynomials. Although the conventional DGM, like the finite element method, use triangle domain to flexibly divide the two-dimensional computational domain, it will result in much complexities in modeling for some objects with the arbitrary shapes including the simple and complex shapes.

In this paper, we firstly develop a novel technique for discretization of the constitutive equations of LHM; in the following, we derive the modified PML formulae which are stable for the LHM; then we extend the conventional DGM based on the triangle domains to the new DGM based on hybrid domains, i.e., triangle domains and quadrilateral domains; finally we adopt the new DGM with the modified PML formulae to analyze the unusual electromagnetic phenomena properties of the LHM.

2. DISCRETE MODEL FOR MATERIAL EQUATIONS OF THE LHM

2.1. Maxwell's Equations in the LHM

We adopt the idea of the Lorentz medium used to simulate the negative ε and μ. Note that by simply imposing ε and μ negative inside the LHM would produce an unstable simulation, since the field at the interface between the LHM and air media, for a matched case, would blow up. Hence, the Lorentz medium approach is more general and can be applied to both matched and unmatched interfaces.

The constitutive relations for a frequency dispersive isotropic medium read as follows:

$$\begin{cases} \vec{D} = \varepsilon(\omega)\vec{E} \\ \vec{B} = \mu(\omega)\vec{H} \end{cases} \tag{3}$$

Negative permittivity and permeability are realized with the Lorentz medium model. The expressions for the permittivity and permeability are of the form

$$\begin{cases} \varepsilon(\omega) = \varepsilon_0 \left(1 + \dfrac{\omega_{pe}^2}{\omega_{oe}^2 - \omega^2 + j\Gamma_e\omega}\right) \\ \mu(\omega) = \mu_0 \left(1 + \dfrac{\omega_{pm}^2}{\omega_{om}^2 - \omega^2 + j\Gamma_m\omega}\right) \end{cases} \tag{4}$$

This model corresponds to a realization of DNG materials as mixtures of conductive spirals or omega particles [18]. Substituting those expressions into 2-D TM_z (transverse magnetic to z) polarization Maxwell's equations in the frequency domain, we can obtain

$$j\omega E_z = \frac{1}{\varepsilon_0}\left(\frac{\partial H_y}{\partial x} - \frac{\partial H_x}{\partial y}\right) - S_z \tag{5}$$

$$j\omega H_x = -\frac{1}{\mu_0}\frac{\partial E_z}{\partial y} - G_x \tag{6}$$

$$j\omega H_y = \frac{1}{\mu_0}\frac{\partial E_z}{\partial x} - G_y \tag{7}$$

where

$$j\omega S_z = \omega_{pe}^2 E_z - \Gamma_e S_z - \omega_{oe}^2 R_z \tag{8}$$

$$j\omega R_z = S_z \tag{9}$$

$$j\omega G_x = \omega_{pm}^2 H_x - \Gamma_m G_x - \omega_{om}^2 F_x \tag{10}$$

$$j\omega F_x = G_x \tag{11}$$

$$j\omega G_y = \omega_{pm}^2 H_y - \Gamma_m G_y - \omega_{om}^2 F_y \tag{12}$$

$$j\omega F_y = G_y \tag{13}$$

2.2. Modified PML for LHM

In the LHM, the direction of phase velocity is contrary to the direction of power flow because of the simultaneously negative permittivity and permeability. In this case, standard versions of PML [10, 11] have been shown to be numerically unstable [19, 20] when they are extended to truncate the boundary of LHM. In order to derive the stable PML for LHM, we adopt the Nearly Perfectly Matched Layer (NPML) [21] based on the modified complex coordinate stretching variables.

We modify the original complex coordinate stretching variables [22, 23] as following:

$$\begin{aligned} \partial x &\Rightarrow 1 + \frac{w_x}{j\omega\left(1 + \dfrac{\omega_{pe}^2}{\omega_{oe}^2 - \omega^2 + j\omega\Gamma_e}\right)}\partial x \\ \partial y &\Rightarrow 1 + \frac{w_y}{j\omega\left(1 + \dfrac{\omega_{pe}^2}{\omega_{oe}^2 - \omega^2 + j\omega\Gamma_e}\right)}\partial y \end{aligned} \tag{14}$$

Applying (14) into (5) and redefining new field variables

$$\begin{aligned}\tilde{H}_x &= \frac{1}{1+\dfrac{w_y}{j\omega\left(1+\dfrac{\omega_{pe}^2}{\omega_{oe}^2-\omega^2+j\omega\Gamma_e}\right)}}H_x \\ \tilde{H}_y &= \frac{1}{1+\dfrac{w_x}{j\omega\left(1+\dfrac{\omega_{pe}^2}{\omega_{oe}^2-\omega^2+j\omega\Gamma_e}\right)}}H_y\end{aligned} \tag{15}$$

and transforming them into time domain, we can obtain the equation of NPML as following:

$$\frac{\partial E_z}{\partial t} = \frac{1}{\varepsilon_0}\left(\frac{\partial \tilde{H}_y}{\partial x}-\frac{\partial \tilde{H}_x}{\partial y}\right)-S_z \tag{16}$$

$$\tilde{H}_y = H_y - w_x P_y \tag{17}$$

$$\frac{\partial P_y}{\partial t} = \tilde{H}_y - \omega_{pe}^2 Q_y \tag{18}$$

$$\frac{\partial Q_y}{\partial t} = P_y - \omega_{oe}^2 U_y - \Gamma_e Q_y \tag{19}$$

$$\frac{\partial U_y}{\partial t} = Q_y \tag{20}$$

$$\tilde{H}_x = H_x - w_y P_x \tag{21}$$

$$\frac{\partial P_x}{\partial t} = \tilde{H}_x - \omega_{pe}^2 Q_x \tag{22}$$

$$\frac{\partial Q_x}{\partial t} = P_x - \omega_{oe}^2 U_x - \Gamma_e Q_x \tag{23}$$

$$\frac{\partial U_x}{\partial t} = Q_x \tag{24}$$

The variable changes in (15) are not strictly correct because w_s ($s = x, y$) is s-dependent. Based on the approximation in derivation, corresponding PML is called as NPML [21]. It is noted that the performance of NPML will not be affected by the approximation [24].

Similarly for (6) and (7), new field variables in PML are defined

as

$$\begin{aligned}\tilde{E}_{z1} &= \frac{1}{1+\dfrac{w_y}{j\omega\left(1+\dfrac{\omega_{pe}^2}{\omega_{oe}^2-\omega^2+j\omega\Gamma_e}\right)}}E_z \\ \tilde{E}_{z2} &= \frac{1}{1+\dfrac{w_x}{j\omega\left(1+\dfrac{\omega_{pe}^2}{\omega_{oe}^2-\omega^2+j\omega\Gamma_e}\right)}}E_z\end{aligned} \tag{25}$$

Introducing (14) and (25) into (6) and (7) and transforming them into time domain, we can obtain

$$\frac{\partial H_x}{\partial t} = -\frac{1}{\mu_0}\frac{\partial \tilde{E}_{z1}}{\partial y} - G_x \tag{26}$$

$$\tilde{E}_{z1} = E_z - w_y D_{z1} \tag{27}$$

$$\frac{\partial D_{z1}}{\partial t} = \tilde{E}_{z1} - \omega_{pe}^2 B_{z1} \tag{28}$$

$$\frac{\partial B_{z1}}{\partial t} = D_{z1} - \omega_{oe}^2 C_{z1} - \Gamma_e B_{z1} \tag{29}$$

$$\frac{\partial C_{z1}}{\partial t} = B_{z1} \tag{30}$$

$$\frac{\partial H_y}{\partial t} = \frac{1}{\mu_0}\frac{\partial \tilde{E}_{z2}}{\partial x} - G_y \tag{31}$$

$$\tilde{E}_{z2} = E_z - w_x D_{z2} \tag{32}$$

$$\frac{\partial D_{z2}}{\partial t} = \tilde{E}_{z2} - \omega_{pe}^2 B_{z2} \tag{33}$$

$$\frac{\partial B_{z2}}{\partial t} = D_{z2} - \omega_{oe}^2 C_{z2} - \Gamma_e B_{z2} \tag{34}$$

$$\frac{\partial C_{z2}}{\partial t} = B_{z2} \tag{35}$$

It is noted that due to the adoption of approximation, the PML formulations are weak well-posedness of the Maxwell's equation system [25], although the PML formulations has the unsplit-field form. However, the property which many PML formulations have does not appear to be an issue of practical importance in ordinary problems.

2.3. Discontinuous Galerkin Method

We shall seek approximate solutions to Maxwell's equations in a general domain, Ω, containing a collection of scattering bodies. Here, we start by assuming that the computational domain, Ω, is decomposed into curvilinear triangle domains and quadrilateral domains, as illustrated in Fig. 1.

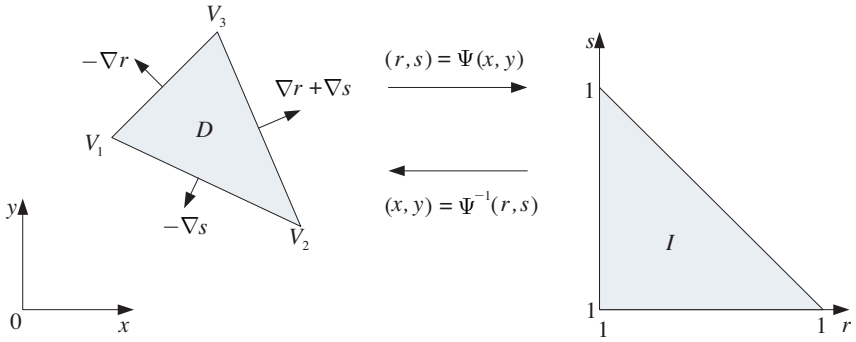

(a) mapping between the general curvilinear triangle, D, and the triangle, I

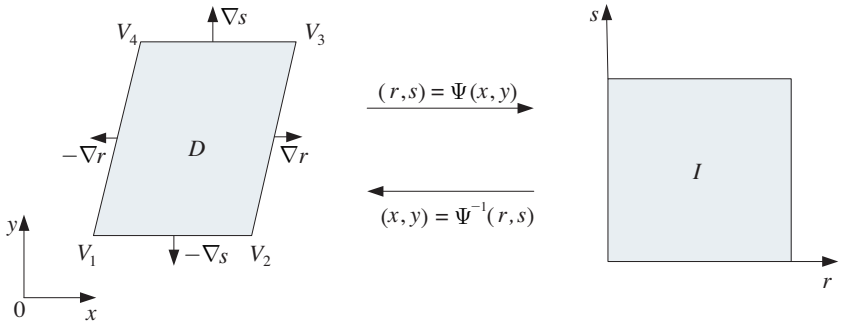

(b) mapping between the general curvilinear quadrilateral, D, and the square, I

Figure 1. Mapping between the general domains and the standard domains.

The number of grid points needed per triangle is

$$N = \frac{(n+1)(n+2)}{2} \tag{36}$$

which also becomes the number of local unknowns. For per quadrilateral domain, the number of grid points is

$$N = (n+1)(n+1) \tag{37}$$

in which n is the order of the local polynomial approximation.

We shall assume the existence of a mapping relation which maps the standard right angle triangle to the triangle domain. Assuming for simplicity that the triangle domain is straightsided, this mapping is simply given as

$$x(r,s) = -\frac{r+s}{2}v_1 + \frac{1+r}{2}v_2 + \frac{1+s}{2}v_3 \tag{38}$$

where $v_1 = (x_1, y_1),\ v_2(x_2, y_2),\ v_3 = (x_3, y_3)$ are the vertex coordinates of the triangle domain. Likewise, the mapping relation between the square and the straightsided quadrilateral is given as

$$x(r,s) = \frac{1-r}{2}\frac{1-s}{2}v_1 + \frac{1+r}{2}\frac{1-s}{2}v_2 + \frac{1+r}{2}\frac{1+s}{2}v_3 + \frac{1-r}{2}\frac{1+s}{2}v_4 \tag{39}$$

in which $v_1 = (x_1, y_1),\ v_2 = (x_2, y_2),\ v_3 = (x_3, y_3),\ v_4 = (x_4, y_4)$ are the vertex coordinates of the quadrilateral domain.

The choice of the nodal distributions inside the triangle has received some attention recently. The distributions, allowing for the construction of well behaved unique Lagrange polynomials up to order 19, can be found [26]. There are exactly N grid points in a triangle and, furthermore, the nodes along the edges are the one dimensional Legendre-Guass-Lobatto points. Fig. 2(a) shows the grid point distributions with $n = 10,\ N = 66$. In order to correctly connect between quadrilateral and triangle, the nodal distributions is chosen as Legendre-Guass-Lobatto points in the quadrilateral, as shown in Fig. 2(b).

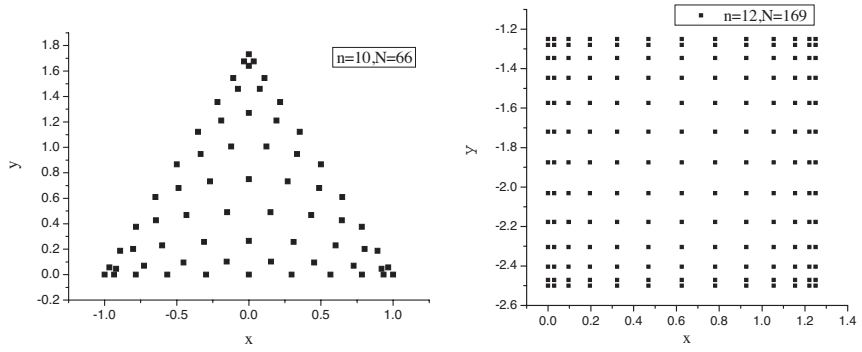

(a) grid point distributions in the triangle (b) grid point distributions in the quadrilateral

Figure 2. Examples of nodal distributions in the triangle and the quadrilateral.

An orthonormal basis on the triangle is given as

$$\tilde{\psi}_i(r) = P_{\alpha_1}^{(0,0)}\left(\frac{2(r+1)}{(1-s)} - 1\right)\left(\frac{1-s}{2}\right)^{\alpha_1} P_{\alpha_2}^{(2\alpha_1+1.0)}(s) \tag{40}$$

$$i = \alpha_1 + n\alpha_2 - \frac{\alpha_2}{2}(-1+\alpha_2) + 1 \tag{41}$$

$$\gamma_i = \left(\frac{2}{2\alpha_1+1}\right)\left(\frac{1}{\alpha_1+\alpha_2+1}\right) \tag{42}$$

$$\psi_i(r) = \frac{\tilde{\psi}_i(r)}{\sqrt{\gamma_i}} \tag{43}$$

$P_n^{(\alpha_1,\alpha_2)}(x)$ represents the classical Jacobi polynomial of order n, e.g., $P_n^{(0,0)}(x)$ is the Legendre polynomial. Similarly, the orthonormal basis on the quadrilateral is given as

$$\tilde{\psi}_{\alpha_1\alpha_2}(r) = P_{\alpha_1}^{(0,0)}(r)P_{\alpha_2}^{(0,0)}(s) \tag{44}$$

$$\gamma_{\alpha_1\alpha_2} = \left(\frac{2}{2\alpha_1+1}\right)\left(\frac{1}{2\alpha_2+1}\right) \tag{45}$$

$$\psi_{\alpha_1\alpha_2}(r) = \frac{\tilde{\psi}_{\alpha_1\alpha_2}(r)}{\sqrt{\gamma_{\alpha_1\alpha_2}}} \tag{46}$$

We write two-dimensional Maxwell's equations as a conservation law

$$Q\frac{\partial q}{\partial t} + \nabla \cdot F(q) = 0 \tag{47}$$

where Q represent the materials, q the 3-vector of fields and $F(q)$ the flux. The detailed definition of these depends on which polarization is considered, i.e., for the TM_z form, we have

$$Q = \begin{bmatrix} \mu & 0 & 0 \\ 0 & \mu & 0 \\ 0 & 0 & \varepsilon \end{bmatrix}, \quad q = \begin{bmatrix} H_x \\ H_y \\ E_z \end{bmatrix}, \quad F(q) = \begin{bmatrix} 0 & E_z \\ -E_z & 0 \\ H_y & H_x \end{bmatrix} \tag{48}$$

In kth subdomain, we shall assume that the solution q^k can be expressed as a polynomial approximation

$$q_N^k(x,t) = \sum_{i=1}^{N} q^k\left(x_i^k, t\right)(x^k) \tag{49}$$

where $L_i^k(x^k)$ is the multidimensional Lagrange polynomial. To arrive at the semi-discrete scheme, let us require that local residual, i.e., the

error when $q_N^k(x,t)$ is substituted in to (19), vanishes in the following way

$$\forall k : \int_{D_k} \left(Q\frac{\partial q_N^k}{\partial t} + \nabla \cdot F_N^k \right) L_i^k(x^k) dx^k = \oint_{\partial D^k} L_i^k(x^k) \hat{n} \cdot \left[F_N^k - F^* \right] dx^k \tag{50}$$

where the normal unit vector $\hat{n}$ is pointing out of the boundary of the kth subdomain.

This can be recognized as a Galerkin approach, albeit on the local element only. The numerical flux, $\hat{n} \cdot F^*$, can be obtained by Rankine-Hugonoit jump conditions to satisfy the following relation [27]

$$\hat{n} \cdot [F - F^*] = \begin{cases} \overline{Z}^{-1} \hat{n} \times \left(-Z^+ [\vec{H}] + \hat{n} \times [\vec{E}] \right) \\ \overline{Y}^{-1} \hat{n} \times \left(Y^+ [\vec{E}] + \hat{n} \times [\vec{H}] \right) \end{cases} \tag{51}$$

where $[\vec{E}] = \vec{E}^- - \vec{E}^+$ and $[\vec{H}] = \vec{H}^- - \vec{H}^+$ measure the jumps in the field values across the interface and superscript '+' and '−' refer to the values from neighbor and local element, respectively. Here parameters $Z^\pm$ and $Y^\pm$ denote the impedance and the conductance of the medium, respectively, and $\overline{Z}$ and $\overline{Y}$ are the sums of the local impedance and conductance, respectively.

This suffices to write down the local two-dimensional scheme for TM_z scheme as

$$\varepsilon^k M^{2d} \frac{\partial E_z^k}{\partial t} - S_x H_y^k + S_y H_x^k = F\left\{ \hat{z} \cdot \left[\overline{Y}^{-1} \hat{n} \times \left(Y^+ [\vec{E}] + \hat{n} \times [\vec{H}] \right) \right] \right\}\Big|_{\partial D^k} \tag{52}$$

$$\mu^k M^{2d} \frac{\partial H_x^k}{\partial t} + S_y E_z^k = F\left\{ \hat{x} \cdot \left[\overline{Z}^{-1} \hat{n} \times \left(-Z^+ [\vec{H}] + \hat{n} \times [\vec{E}] \right) \right] \right\}\Big|_{\partial D^k} \tag{53}$$

$$\mu^k M^{2d} \frac{\partial H_y^k}{\partial t} - S_x E_z^k = F\left\{ \hat{y} \cdot \left[\overline{Z}^{-1} \hat{n} \times \left(-Z^+ [\vec{H}] + \hat{n} \times [\vec{E}] \right) \right] \right\}\Big|_{\partial D^k} \tag{54}$$

where M_{2d} represents the local mass matrix; S_x and S_y represents the stiffness matrix; F represents edge operator. They are given as respectively

$$\begin{aligned} M^{2d}\Big|_{ij} &= \left(L_i(x^k), L_j(x^k) \right)_{D^k} \quad F\Big|_{ij} = \left(L_i(x^k), L_j(x^k) \right)_{\partial D^k} \\ S_x\Big|_{ij} &= \hat{x} \cdot \left(L_i(x^k), \nabla L_j(x^k) \right)_{D^k} \quad S_y\Big|_{ij} = \hat{y} \cdot \left(L_i(x^k), \nabla L_j(x^k) \right)_{D^k} \end{aligned} \tag{55}$$

3. NUMERICAL RESULTS

Having developed the formulations for the time domain solution of the LHM, it is now time to consider the actual performance of the computational framework. Temporal integration of the semidiscrete approximation is done using a fourth-order, five-stage low storage Runge-Kutta scheme [28] and a stability-limit time step scaling as

$$\Delta t \leq \mathrm{CFL} \min_{\Omega} \sqrt{\varepsilon_r \mu_r} |\chi|^{-1} \tag{56}$$

with $\sqrt{\varepsilon_r \mu_r}$ reflecting the modified local speed of light due to materials and

$$|\chi| = \frac{|\nabla r|}{\Delta r} + \frac{|\nabla s|}{\Delta s} \tag{57}$$

Here $|\cdot|$ refers to the absolute value of each of the vector components, i.e., $|\nabla r| = [|r_x| \quad |r_y|]^T$; $(\Delta r, \Delta s)$ measures the axial distance separating neighboring nodal points in I. Hence χ provides a measure of the local grid distortion as a consequence of the mapping.

Two kinds of excitation sources are considered in this work: uniform plane wave and localized lined source. For the uniform plane source, the time function is chosen as the Blackman-Harris window function [29] which can be expressed as

$$f(t) = \begin{cases} -\sum_{n=1}^{3} \dfrac{n\pi}{T} a_n \sin\left(\dfrac{2n\pi t}{T}\right), & 0 < t < T \\ 0 & \text{otherwise} \end{cases} \tag{58}$$

where $a_1 = -0.488$, $a_2 = 0.145$, $a_3 = -0.01022222$. The center frequency of this function is defined as $f_c = 1.55/T$. For localized lined source, the time function is chosen as the multiple cycle m-n-m pulse [8] which can be expressed as

$$f(t) = \begin{cases} g_{on}(t) \sin(\omega_0 t) & 0 \leq t < mT_p \\ \sin(\omega_0 t) & mT_p \leq t \leq (m+n)T_p \\ g_{off}(t) \sin(\omega_0 t) & (m+n)T_p \leq t \leq (m+n+m)T_p \\ 0 & (m+n+m)T \leq t \end{cases} \tag{59}$$

where $T_p = 1/f_0$ is the period of one single cycle and the three-derivative smooth window functions are given by

$$\begin{cases} g_{on}(t) = 10x_{on}^3 - 15x_{on}^4 + 6x_{on}^5 \\ g_{off}(t) = 1 - \left(10x_{off}^3 - 15x_{off}^4 + 6x_{off}^5\right) \end{cases} \tag{60}$$

with

$$\begin{cases} x_{on} = 1 - (mT_p - t)/mT_p \\ x_{off} = (t - (m+n)T_p)/mT_p \end{cases} \tag{61}$$

The multiple cycle m-n-m pulse is a sinusoidal signal that has a smooth windowed turn-on for m cycles, a constant amplitude for n cycles, and then a smooth windowed turn-off for m cycles; hence, it has an adjustable bandwidth (through the total number of cycles $m+n+m$) centered at the frequency f_0, as shown in Fig. 3.

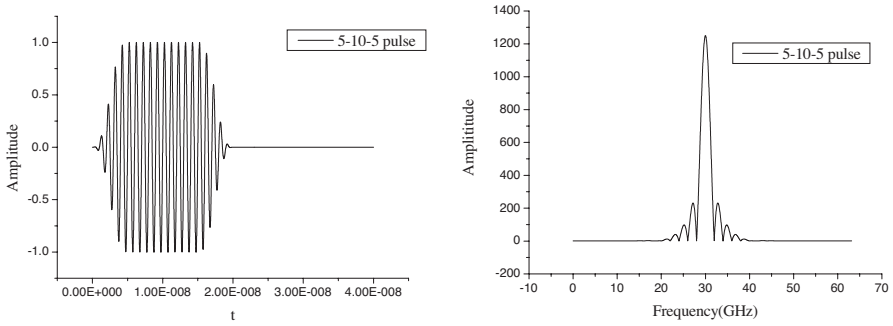

Figure 3. The waveform of the line electric current source in time domain and frequency domain.

In addition, the Matrix-Pencil method [30] is used to reduce the required computing time to reach the harmonic steady state.

Firstly, we test the validity and accuracy of the DGM based on hybrid subdomains and the modified PML we proposed in the paper. Consider plane wave scattering from a perfect conducting cylinder in free space, as shown in Fig. 4(a). The modified PML is used to truncate the boundary of computational domain. A plane wave is incident along the x-axis on the cylinder. The radius of perfect conducting cylinder is $2m$. In our calculation $\Delta t = 1\,\text{ps}$ and the observation point is located at $(-2.1036, -2.1036)$. The solution to the scattering electric field E_z at the observation point and the analytical solution are compared as shown in Fig. 4(b). The excellent agreement of the results shows the validity and accuracy of our algorithm.

For the second example, we validate the effectiveness of PML we proposed in the paper. The geometry of computational domain is shown in Fig. 5(a). The perfectly matched layer absorbing boundary condition is extended to truncate the boundary of left-handed materials in DGM simulation. A line electric current and observation point are located at $(-0.02, 0.0)$ m and $(0.0, -0.0476)$ m, respectively. The center frequency of the source is 30 GHz. The parameters in (4) are as follows:

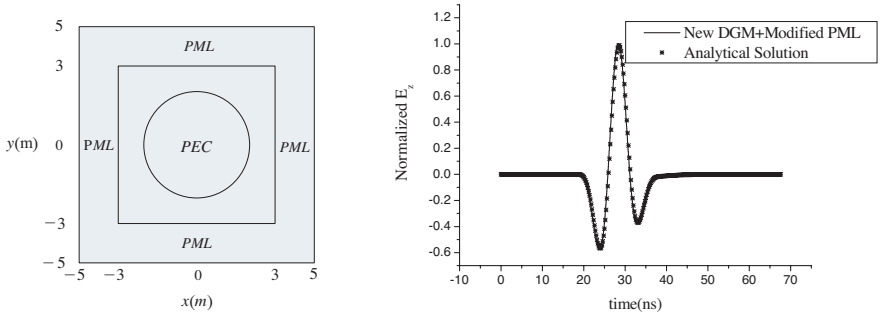

(a) geometry (b) comparison of the DGM result with the analytical solution

Figure 4. Plane wave scattering from a PEC circular cylinder in free space.

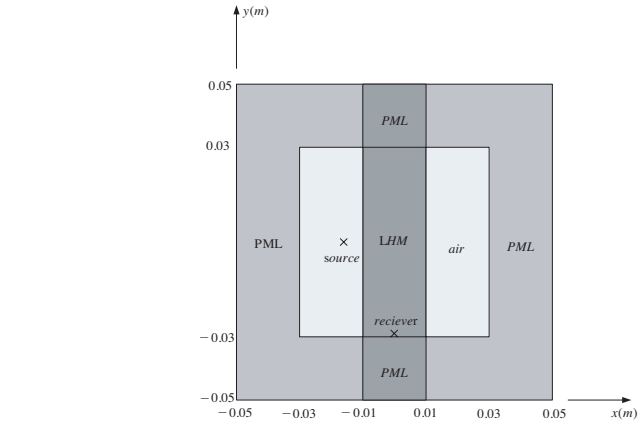

(a) The geometry of computational domain

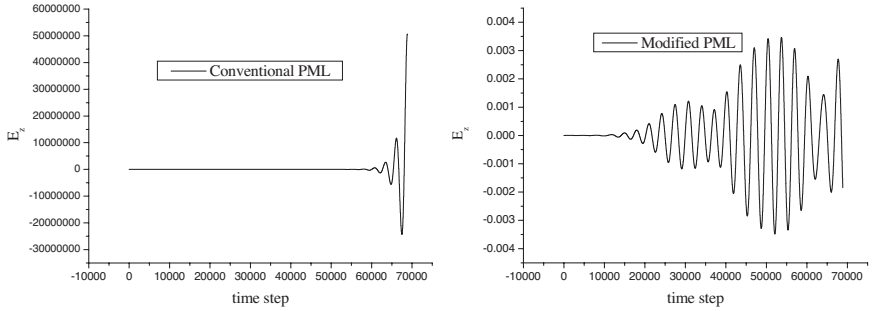

(b) The unstable time domain field for the standard PML (c) The stable time domain field for the modified PML

Figure 5. The comparison of performance between the standard PML simulation and the modified PML simulation.

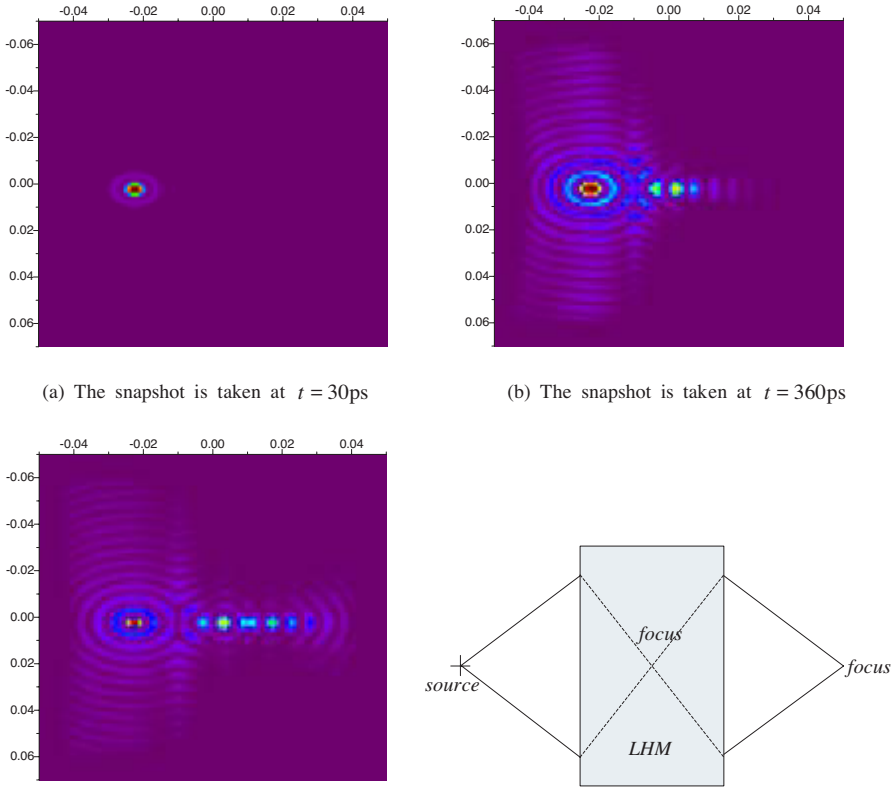

(a) The snapshot is taken at $t = 30$ps

(b) The snapshot is taken at $t = 360$ps

(c) The snapshot is taken at $t = 540$ps

(d) The negative refractive index in the LHM

Figure 6. The simulation of the focus property of LHM.

$\Gamma_e = \Gamma_m = 0$, $\omega_{oe} = \omega_{om} = 0$, $\omega_{pe} = \omega_{pm} = 2.655 \times 10^{11}$ rad/s. In order to ensure the stability of the DGM, the time step Δt is set to be 0.01 ps. As shown in Fig. 5(b) and (c), the DGM with the modified PML and the DGM with the standard PML are adopted to calculate the field E_z at the observation point, respectively. By comparison, we can find that the standard PML simulation is unstable, while the modified PML simulation is stable enough to compute a solution for at least 70000 time steps. Therefore, the stability of the modified PML is greatly better than that of the standard PML, when the PML is extended to truncate the boundary of left-handed materials.

For the third example, we consider the perfect lens foci property of the LHM. The geometry and the parameter of the LHM are similar to those in the example above. The center frequency of line electric

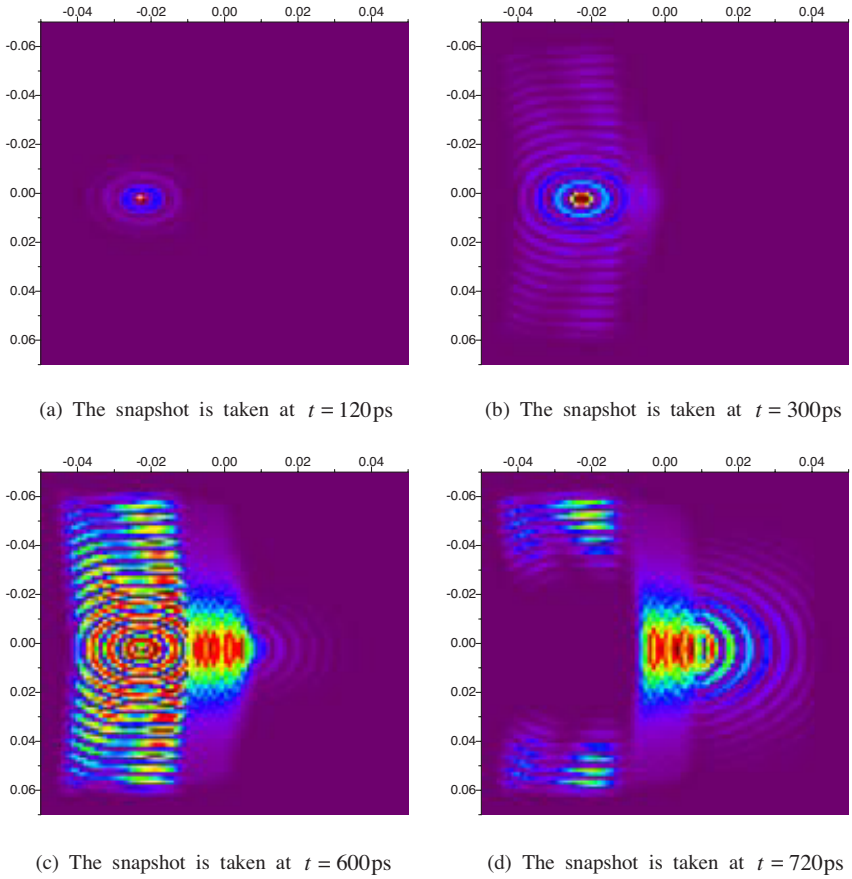

(a) The snapshot is taken at $t = 120$ ps

(b) The snapshot is taken at $t = 300$ ps

(c) The snapshot is taken at $t = 600$ ps

(d) The snapshot is taken at $t = 720$ ps

Figure 7. The simulation of paraxial foci property of LHM.

current source is set to be 30 GHz, and its time function is the 5-10-5 pulse. The snapshots of electric field intensity over the whole simulation space are taken at $t = 30$ ps, 360 ps, 540 ps. The focus inside and outside the LHM slab can be seen, as shown in Fig. 6(b) and (c). This is because of the negative refractive index in the LHM [8], as shown in Fig. 6(d). It is noted that there are no steady state foci because of the highly dispersive nature of the LHM. In this example, because the PML ABC is extended to truncate the boundary of the LHM, we accurately model the LHM slab of infinite in y-axis.

Next, we consider the paraxial foci property of LHM. The geometry and the source setting are similar to those in the second example. The parameters in (4) are as follows: $\Gamma_e = \Gamma_m = 1.0 \times$

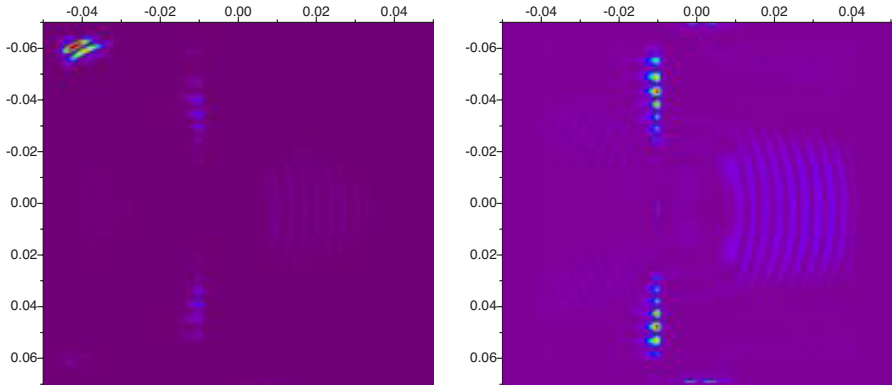

(a) The snapshot is taken at $t = 900$ps (b) The snapshot is taken at $t = 960$ps

Figure 8. The simulation of electric field intensity over computational domain for the slab with $\mu < 0,\ \varepsilon > 0$.

10^8 rad/s, $\omega_{oe} = \omega_{om} = 0$. $\omega_{pe} = \omega_{pm} = 5.0 \times 10^{11}$ rad/s. The numerical intensities of electric field in whole computational domain at $t = 120$ ps, 300 ps, 600 ps, 720 ps are plotted in Fig. 7. As shown in Fig. 7(c) and (d), the paraxial focus appears near the center of the LHM slab. This is accordance to the results given in [8]. Furthermore, the paraxial focus beyond the rear face of the LHM slab is very difficult to distinguish from the behavior of the field while the wave exits slab. In this example, we can find that effect of fringe fields caused by the top and bottom edges of the LHM slab has been eliminated because PML ABC is extended to truncate the boundary of LHM.

In the following, we consider two cases for a slab with $\mu < 0,\ \varepsilon > 0$, and $\mu > 0,\ \varepsilon < 0$. For the slab with $\mu < 0,\ \varepsilon > 0$, the parameters in (4) are as follows: $\Gamma_e = \Gamma_m = 0$, $\omega_{oe} = \omega_{om} = 0$, $\omega_{pe}^2 = 0$, $\omega_{pm} = 2.655 \times 10^{11}$ rad/s; for the slab with $\mu > 0,\ \varepsilon < 0$, the parameters in (4) are as follows: $\Gamma_e = \Gamma_m = 0$, $\omega_{oe} = \omega_{om} = 0$, $\omega_{pe} = 2.655 \times 10^{11}$ rad/s, $\omega_{pm} = 0$. The center frequency of line electric current source is still set to be 30 GHz. Obviously, the dielectric constant ε and magnetic permeability μ at the center frequency become $\mu = -\mu_0,\ \varepsilon = \varepsilon_0$ for the first case and $\mu = \mu_0,\ \varepsilon = -\varepsilon_0$ for the second case. Fig. 8 and Fig. 9 show the snapshots of electric field intensity over the whole simulation space at $t = 900$ ps, 900 ps for two cases, respectively. In the first case, there are neither real wave vectors nor backward waves because of $\mu < 0,\ \varepsilon > 0$ [6]. It was found that the wave decay exponentially everywhere inside the slab and the surface wave is easily excited on the

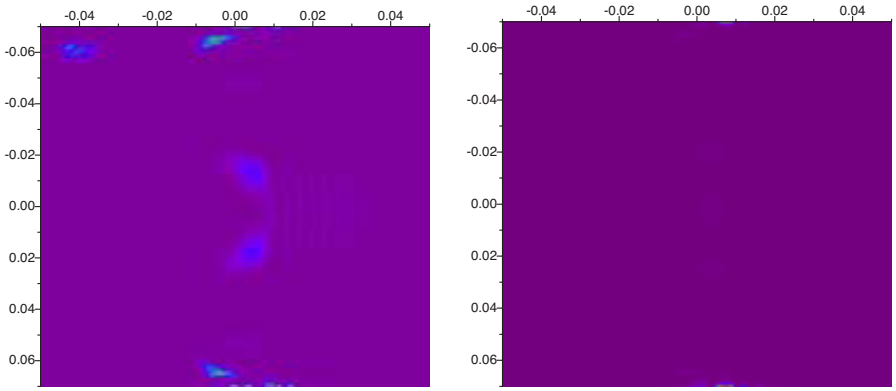

(a) The snapshot is taken at $t = 900$ps (b) The snapshot is taken at $t = 960$ps

Figure 9. The simulation of electric field intensity over computational domain for the slab with $\mu > 0,\ \varepsilon < 0$.

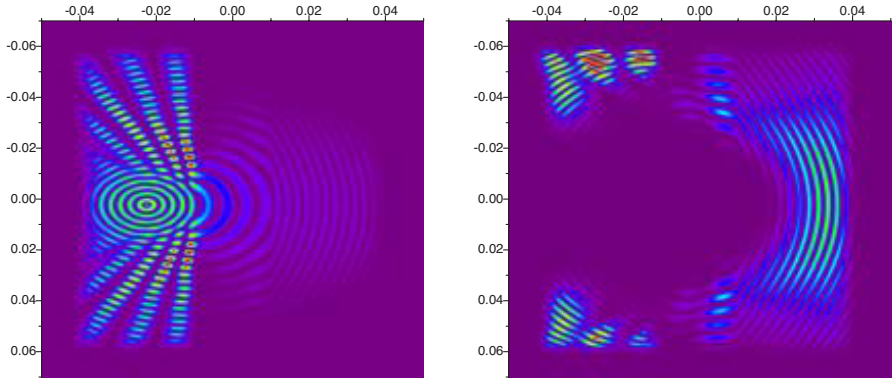

(a) The snapshot is taken at $t = 300$ps (b) The snapshot is taken at $t = 480$ps

Figure 10. The simulation of electric field intensity over computational domain for the slab with $\mu > 0,\ \varepsilon < 0$.

interface, as shown in Fig. 8. In the second case, due to $\mu > 0,\ \varepsilon < 0$, there are still neither real wave vectors nor backward waves [6]. Similar to the first case, the wave decays exponentially everywhere inside the slab. The surface wave, however, is negligible on the surface.

Finally, we consider variation of EM phenomenon in the slab with the center frequency of a line electric current. The medium parameters in the slab are same as those in the second example. Here,

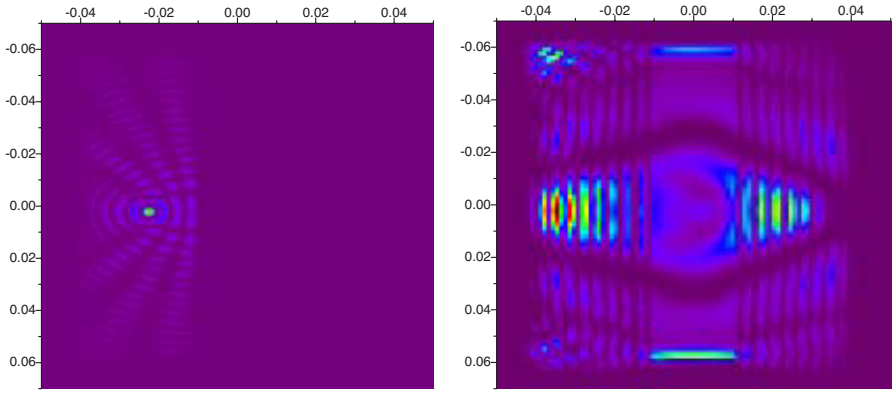

(a) The snapshot is taken at t = 300ps (b) The snapshot is taken at t = 660ps

Figure 11. The simulation of electric field intensity over computational domain for the slab with $\varepsilon = \mu = 0$.

we choose the center frequency of a line electric current as 59.76 GHz and 42.26 GHz, respectively. In the first case, the permittivity ε and permeability μ are positive in the whole frequency band of the excitation. In the second case, the ε and μ are equal to zero at the center frequency. Therefore, the ε and μ are positive in one half of frequency band and the ε and μ are negative in the other half of frequency band. Fig. 10 shows the snapshots of electric field intensity over the whole simulation space at $t = 300$ ps, 480 ps for the first case and Fig. 11 shows the snapshots of electric field intensity over the whole simulation space at $t = 300$ ps, 660 ps for the second case. From Fig. 10 and Fig. 11, we can see that with the change of the center frequency of the excitation from 59.76 GHz to 42.26 GHz, the electromagnetic wave in the slab is converged. Furthermore, when the center frequency becomes 30 GHz, which corresponds to ε and μ with negative values, the electromagnetic wave in the slab is focused at the one point, as shown in the Fig. 6.

4. CONCLUSION

The novel discretization formulations of the Lorentz medium model for the solution of wave propagation in the Left-Handed medium have been developed in this paper. The modified perfectly matched layer formulae have been derived to overcome the instability inherent in the standard PML for the truncating the boundary of left-handed

medium. Furthermore, we adopt discontinuous Galerkin method based on the hybrid domain, i.e. triangle domain and quadrilateral domain, and the modified PML formulae to numerically study EM phenomena in the LHM. The simulation results show accuracy and stability of the proposed scheme and provide a basis for the more research on properties of the left-handed medium.

REFERENCES

1. Veselago, V. G., "The electrodynamics of substances with simultaneously negative values of ε and μ," *Sov. Phys. Usp.*, Vol. 10, 509–515, 1968.
2. Pendry, J. P., A. J. Holden, D. J. Robbins, and W. J. Stewart, "Low frequency plasmons in thin-wire structures," *J. Phys. Condens. Matter.*, Vol. 10, 4785–4809, 1998.
3. Pendry, J. P., A. J. Holden, D. J. Robbins, and W. J. Stewart, "Magnetism from conductors and enhanced nonlinear phenomena," *IEEE Trans. Microwave Theory Tech.*, Vol. MTT-47, 2075–2084, 1999.
4. Smith, D. R., D. C. Vier, W. Padilla, S. C. Nemat-Nasser, and S. Schultz, "Loop-wire medium for investigating plasmons at microwave frequencies," *Appl. Phys. Lett.*, Vol. 75, 1425–1427, 1999.
5. Smith, D. R. and N. Kroll, "Negative refractive index in left-handed materials," *Phys. Rev. Lett.*, Vol. 85, 2933–2936, 2000.
6. Karkkainen, M. K., "Numerical study of wave propagation in uniaxially anisotropic lorentzian backward-wave slabs," *Physical Review E*, Vol. 68, 2003.
7. Karkkainen, M. K., and S. I. Maslovski, "Wave propagation, refraction, and focusing phenomena in Lorentzian double-negative materials: a theoretical and numerical study," *Microwave Opt. Technol. Lett.*, Vol. 37, 4–7, 2003.
8. Ziolkowski, R. W. and E. Heyman, "Wave propagation in media having negative permittivity and permeability," *Phys. Rev. E*, Vol. 64, 2001.
9. Correia, D. and J. M. Jin, "3D-FDTD-PML analysis of left-handed metamaterials," *Microwave Opt. Technol. Lett.*, Vol. 40, 201–205, 2004.
10. Berenger, J. P., "A perfectly matched layer for absorption of electromagnetic waves," *J. Comput. Phys.*, Vol. 114, 185–200, 1994.

11. Gedney, S. D., "An anisotropic PML absorbing media for the FDTD simulation of fields in lossy and dispersive media," *Electromagn.*, Vol. 16, 399–415, 1996.
12. Cockburn, B. and C. W. Shu, "The local discontinuous Galerkin finite element method for convection-diffusion systems," *SIAM J. Numer. Anal.*, Vol. 35, 1998.
13. LeSaint, P. and P. A. Raviart, "On a finite element method for solving the neutron transport equation," *Mathematical Aspects of Finite Elements in Partial Differential Equations*, C. De. Boor (ed.), 89, Academic Press, New York, 1974.
14. Hesthaven, J. S. and T. Warburton, "High-order nodal methods on unstructured grids. I. Time-domain solution of Maxwell's equations," *J. Comput. Phys.*, Vol. 181, 186–221, 2002.
15. Hesthaven, J. S. and T. Warburton, "High-order accurate methods for time-domain electromagnetics," *Comput. Model. Engin. Sci.*, Vol. 28, 259–279, 2003.
16. Lu, T., P. Zhang, and W. Cai, "Discontinuous Galerkin methods for dispersive and lossy Maxwell's equations and PML boundary conditions," *J. Comput. Phys.*, Vol. 200, 549–580, 2004.
17. Kopriva, D., S. L. Woodruff, and M. Y. Hussaini, "Discontinuous spectral element approximation of Maxwell's equations," *Discontinuous Galerkin Methods: Theory, Computation and Applications*, B. Cockburn, G. Karniadakis, and C.-W. Shu (eds.), 451, Springer-Verlag, New York, 2000.
18. Tretyakov, S. A., I. S. Nefedov, C. R. Simovski, and S. I. Maslovski, "Advances in electromagnetics of complex media and metamaterials," *NATO-ARW Proceedings*, Kluwer, 2002.
19. Dong, X. T., X. S. Rao, Y. B. Gan, B. Guo, and W. Y. Yin, "Perfectly matched layer-absorbing boundary condition for left-handed materials," *IEEE Microwave Wireless Compon. Lett.*, Vol. 14, 301–303, 2004.
20. Cummer, S. A., "Perfectly matched layer behavior in negative refractive index materials," *IEEE Antenna Wireless Propagat. Lett.*, Vol. 3, 172–175, 2004.
21. Cummer, S. A., "A simple, nearly perfectly matched layer for general electromagnetic media," *IEEE Microwave Wireless Compon. Lett.*, Vol. 13, 128–130, 2003.
22. Chew, W. C. and W. H. Weedon, "A 3D perfectly matched medium from modified Maxwell's equation with stretched coordinates," *Microwave Opt. Technol. Lett.*, Vol. 7, 599–604, 1994.

23. Fan, G. X. and Q. H. Liu, "A well-posed PML absorbing boundary condition for lossy media," *IEEE Antennas Propagation Soc. Int. Symp.*, Vol. 3, 2–5, 2001.
24. Berenger, J. P., "On the reflection from Cummer's nearly perfectly matched layer," *IEEE Microwave Wireless Compon. Lett.*, Vol. 14, 334–336, 2004.
25. Abarbanel, S. and D. Gottlieb, "A mathematical analysis of the PML method," *J. Comput. Phys.*, Vol. 134, 357–363, 1997.
26. Hesthaven, J. S., "From electrostatics to almost optimal nodal stes for polynomial interpolation in a simplex," *SIAM J. Numer. Anal.*, Vol. 35, 655–676, 1998.
27. Mohammadian, A. H., V. Shankar, and W. F. Hall, "Computation of electromagnetic scattering and radiation using a time-domain finite-volume discretization procedure," *Comput. Phys. Communications*, Vol. 68, 175–196, 1991.
28. Carpenter, M. H. and C. A. Kennedy, "Fourth order 2N-storage Runge-Kutta scheme," NASA, NASA-TM-109112, 1994.
29. Liu, Q. H., The PSTD algorithm: A time-domain method requiring only two cells per wavelength," *Microwave Opt. Technol. Lett.*, Vol. 15, 158–165, 1997.
30. Hua, Y. and T. K. Sarkar, Generalized pencil-of-function method for extracting poles of an EM system from its transient response," *IEEE Trans. Antennas Propagat.*, Vol. AP-37, 229–234, 1989.